Three-Dimensional Imaging of Nerve Tissue by X-Ray Phase-Contrast Microtomography

F. Beckmann,* K. Heise,# B. Kölsch,# U. Bonse,* M. F. Rajewsky,# M. Bartscher,* and T. Biermann*
*Institute of Physics, University of Dortmund, D-44221 Dortmund, Germany, and #Institute of Cell Biology (Cancer Research), University of Essen Medical School, D-45122 Essen, Germany

ABSTRACT We show that promising information about the three-dimensional (3D) structure of a peripheral nerve can be obtained by x-ray phase-contrast microtomography (p-μCT; Beckmann, F., U. Bonse, F. Busch, and O. Günnewig, 1997. *J. Comp. Assist. Tomogr.* 21:539–553). P-μCT measures electronic charge density, which for most substances is proportional to mass density in fairly good approximation. *The true point-by-point variation of density is thus determined in 3D at presently 1 mg/cm^3 standard error (SE).* The intracranial part of the rat trigeminal nerve analyzed for the presence of early schwannoma "microtumors" displayed a detailed density structure on p-μCT density maps. The average density of brain and nerve tissue was measured to range from 0.990 to 0.994 g/cm^3 and from 1.020 to 1.035 g/cm^3, respectively. The brain-nerve interface was well delineated. Within the nerve tissue, a pattern of nerve fibers could be seen that followed the nerve axis and contrasted against the bulk by 7 to 10 mg/cm^3 density modulation. Based on the fact that regions of tumor growth have an increased number density of cell nuclei, and hence of the higher z element phosphorus, it may become possible to detect very early neural "microtumors" through increases of average density on the order of 10 to 15 mg/cm^3 by using this method.

INTRODUCTION

For histologic structural analyses, 3D imaging is usually superior to 2D histologic sectioning techniques, provided the 3D methods furnish comparable spatial resolution and contrast. Tomography, and in particular x-ray tomography, represents a successful and widely employed 3D imaging method. However, only recently the spatial resolution of x-ray tomography reached the micrometer range as "micro" tomography (μCT) essentially through the use of x-rays generated by synchrotron radiation (SR) sources. The applications of μCT in medicine and biology have recently been reviewed by Bonse and Busch (1996). Unfortunately, conventional x-ray tomography relies on x-ray attenuation contrast and does not give sufficient microstructural information when the specimen contains only light elements, as is the case with many biological and medical tissue samples. For this type of specimens, besides magnetic resonance imaging (MRI), which can be tuned on certain *light* isotopes (e.g., ^{1}H, ^{15}N), the recently developed x-ray phase contrast μCT (p-μCT; Beckmann et al., 1995; Momose et al., 1995; Beckmann, 1998) is a better choice. With p-μCT the *electron charge distribution* in the specimen is imaged, which implies that contrast scales proportional atomic number Z and not $\approx Z^{3.5}$, as in the case of attenuation contrast. Because of the large exponent 3.5 light elements cannot be seen in the presence of heavier ones. We have applied p-μCT to investigate the structure of the intracranial part of the rat trigeminal nerve and describe some of the results in this study.

Received for publication 29 April 1998 and in final form 11 September 1998.

Dedicated to Professor Dr.-Ing. Werner Düchting on the occasion of his 65th birthday.

Address reprint requests to Dr. Ulrich Bonse, Institut für Physik, Universität Dortmund, D-44221 Dortmund, Germany. Tel.: 49-231-7553504; Fax: 49-231-7553657; E-mail: bonse@physik.uni-dortmund.de.

0006-3495/99/01/98/05 $2.00

METHOD OF P-μCT

The specimen is located in one of the two interfering beams (Fig. 1) of an x-ray interferometer (Bonse and Hart, 1965). The interference pattern is modified by the elastic *forward* diffraction of the specimen and recorded as "phase-shift projection" by an x-ray area detector. *Deviated* diffracted beams are eliminated through the Bragg diffraction occurring inside the interferometer. The detector consists of a single-crystal high-density scintillator which converts the x-ray picture to visible light, which is then imaged onto a CCD detector by an optical lens. Since the *outer shape* of the embedded specimen is of no interest it is immersed in a cell fluid with a refracted index matching that of the embedding material as closely as possible. This procedure also reduces the total number P of 2π phase shifts to be measured. For a given specimen of thickness t we have $P \approx t/t_\lambda$, where t_λ is the lambda thickness calculated from Eqs. 2 and 3 using an electron density N_e, which is averaged over the specimen. The maximum number P_{max} of phase "wrap-arounds" that can be handled in the measurement is limited by the condition that consecutive 2π-jumps must not get closer than the given spatial resolution is capable of resolving properly. If the jumps get too close, then by choosing a shorter wavelength λ the phase shift can be reduced. For instance, switching to $\lambda/2$ would halve P.

After data readout, the specimen-induced phase shift is evaluated by means of a special algorithm that eliminates the 2π-ambiguity inherent in the primary interference data. The corrected phase-shift projections are reconstructed using standard methods of tomographic image reconstruction, such as BKFIL (Kak and Slaney, 1987). The result is the desired information about the specimen's 3D "phase structure," i.e., the phase shift $\phi(x, y, z)$ afflicted upon the x-ray wave by a single "voxel" (volume element) as a function of the voxel's position x, y, z in the specimen. From the phase-shift structure the *true 3D point-by-point variation of density* in the specimen is obtained. A detailed description of the method of p-μCT has been given in previous reports (Beckmann et al., 1997; Bonse et al., 1997).

During the measurement, the specimen is immersed in a liquid cell containing a fluid with the refractive index n_f. The reference beam of the interferometer crosses the cell in a specimen-free location. Therefore, $\phi(x, y, z)$ is measured *relative* to the cell fluid.

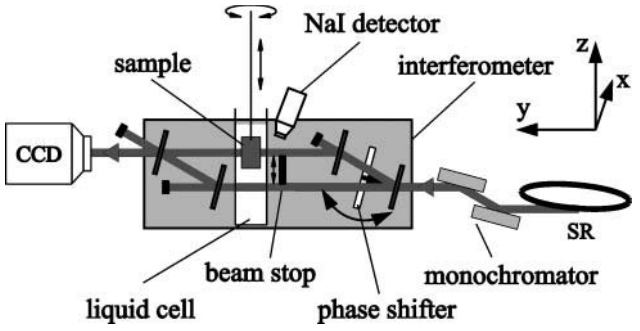

FIGURE 1 Experimental setup for x-ray phase-contrast microtomography. SR is the synchrotron radiation source. The sample is located inside a liquid cell with parallel-sided walls. The average density of the cell fluid is matched to that of the specimen in order to eliminate the influence of the geometrical shape of the specimen on the interference pattern. The setting of the interferometer for maximum intensity of interfering beams is monitored by the NaI detector. Phase contrast can be "switched off" by blocking the lower (reference) beam, thereby allowing for direct comparison of attenuation and phase contrast image.

Denoting with $n_s(x, y, z)$ the x-ray refractive index of the specimen, we obtain

$$\phi(x, y, z) = 2\pi[n_f - n_s(x, y, z)]u/\lambda \quad (1)$$

where u is the voxel size. For x-rays the deviation δ of the refractive index n from one, $\delta \equiv 1 - n$, is a *positive* number, which means that the phase *advances* in a medium, i.e., $\phi(x, y, z) > 0$; δ is of the order of 10^{-6} and given as (James, 1967)

$$\delta(x, y, z) = r_e\lambda^2 N_e(x, y, z)/2\pi \quad (2)$$

where $r_e = 2.8179 \times 10^{-15}$ m is the classic radius of the electron and $N_e(x, y, z)$ the electron density of the material considered as a function of position. A useful quantity giving the material thickness which causes 2π phase shift is the so-called lambda-thickness

$$t_\lambda \equiv \lambda/\delta(x, y, z). \quad (3)$$

By combining Eq. 1 and Eq. 2 we find

$$\phi(x, y, z) = r_e u\lambda[N_{es}(x, y, z) - N_{ef}] \quad (4)$$

$N_{es}(x, y, z)$, N_{ef}, are the electron densities of the specimen and the cell fluid, respectively. Let the specimen (the cell fluid) be composed of S (F) different species of atoms with masses $m_{sk}(x, y, z)$ (m_{fj}), atomic numbers $Z_{sk}(x, y, z)$ (Z_{fj}), and partial mass densities $\rho_{sk}(x, y, z)$ (ρ_{fj}), where $1 \le k \le S$ ($1 \le j \le F$), respectively. With these notations

$$N_{ef} = \sum_{j=1}^{F} Z_{fj}\rho_{fj}/m_{fj} \approx \rho_f/(m_p + m_n + m_e) \quad (5)$$

$$N_{es}(x, y, z) = \sum_{k=1}^{s} Z_{sk}(x, y, z)\rho_{sk}(x, y, z)/m_{sk}(x, y, z) \quad (6a)$$

$$N_{es}(x, y, z) \approx \rho_s(x, y, z)/(m_p + m_n + m_e) \quad (6b)$$

where we have approximated the masses m of atoms by

$$m \approx Z(m_p + m_n + m_e) \quad (7)$$

m_p, m_n, m_e are the masses of proton, neutron, and electron, respectively; ρ_f is the density of the cell fluid and $\rho_s(x, y, z)$ is the (locally varying) density of the specimen. The approximation of Eq. 7 holds to better than 5% for all naturally occurring light elements up to calcium (Z = 20), with the exception of lithium, beryllium, boron, fluorine, and argon, for which the deviations from the approximated mass per unit electron charge are +16%, +13%, +8.1%, +5.5%, and +11%, respectively. A prominent exception is hydrogen, which has no neutron and hence only half the mass per charge than assumed in the approximation. In a specimen of practically uniform mass density, therefore, regions of higher hydrogen concentrations become detectable through increased phase contrast.

Combining Eqs. 4–7, we find

$$\phi(x, y, z) \approx r_e u\lambda[\rho_s(x, y, z) - \rho_f]/(m_p + m_n + m_e) \quad (8)$$

i.e., the phase shift $\phi(x, y, z)$ is directly proportional to the *difference in mass density* of the specimen relative to the cell fluid. To determine the density difference from a measured phase shift $\phi(x, y, z)$ numbers must be introduced for r_e, m_e, m_p, and m_n. Expressing ρ in g/cm^3, $\phi(x, y, z)$ in rad, λ in nm, E in keV, and u in μm, we obtain a formula for easy use in practice:

$$[\rho_s(x, y, z) - \rho_f] = 1.1883 \cdot \phi(x, y, z)/(\lambda u) \quad (9)$$

or, alternatively,

$$[\rho_s(x, y, z) - \rho_f] = 0.9584 \cdot \phi(x, y, z) \cdot (E/u). \quad (10)$$

Throughout the measurements described below we used linseed oil as cell fluid with a density $\rho_f = 0.9305$ g/cm^3 (Neumüller, 1973). Regarding the detection limit for density changes, experiments performed with $E = 12$ keV and $u = 5.4$ μm have shown that at present the *phase* difference $\phi(x, y, z)$ can be measured at 0.5 mrad standard error (SE). Twice this value may be taken as *minimum detectable* phase difference $\phi_{min}(x, y, z)$. Using Eq. 10 we see that this corresponds to a detection limit for *density* differences of ~2 mg/cm^3. With optimized energy, improved overall stability, and better interferometer parameters, we expect that the limit can be decreased to 1 mg/cm^3 in the near future.

The tomograms' spatial resolution has been experimentally determined in two ways: first, by calculating modulation transfer (MTF)-curves from the measured profile generated by a "phase" edge consisting of an aluminum foil of 20 μm thickness in water which, at the employed x-ray energy of 12 keV, yields a phase shift of ~π; and second, by measuring the width of the yellow-violet transition at the boundary nerve/embedding paraffin on pictures such as those shown in Figs. 2 and 3. Both methods yield ~8 μm (15 μm) resolution in x-, y-(z-) direction, respectively. The difference between directions x, y, and z (Fig. 1) is due to the smear caused by the Borrmann fan (Borrmann, 1950) which occurs only in a direction *normal* to the reflecting Bragg planes used in the interferometer.

Specimen Preparation

Intracranial parts of trigeminal nerves were dissected from rats of a (BDIX × BDIV) F_2 cross. Preparation of the nerve tissues included the following steps: fixation in a 4% aqueous solution of formaldehyde (formalin) in phosphate buffer at 4°C for 4 h, further fixation in 4% formalin at room temperature overnight, sequential dehydration in EtOH of increasing concentration (50%, 60%, 70%, 80%, 90%, 96%, and 100%) followed by xylene, and embedding in liquid paraffin at 57°C overnight, casting into paraffin blocks, and solidification at room temperature. This process replaces water by paraffin. Since the relative water content of micro tumor and surrounding tissue is nearly the same (≈80%), the *sign* of eventual density differences present in wet tissues is not altered by dehydration. Furthermore, since the density of paraffin (0.8 mg/cm^3) is *smaller* than that of water, density differences—if altered at all—can only be *enhanced* by dehydration. Therefore, dehydration may increase the chance to discriminate normal and tumor tissue by p-μCT.

Before tomography, histological sections parallel to the nerve axis were made for later comparison with the tomograms. Because of the sectioning, all tomography specimens featured a flat surface mostly oriented parallel to

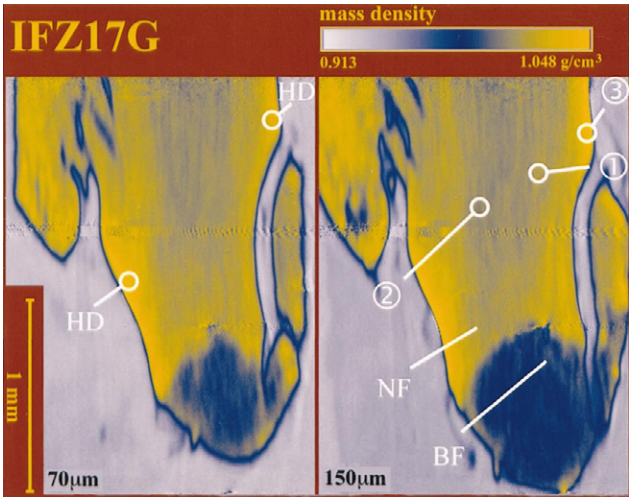

FIGURE 2 Pair of tomograms of the intracranial part of the trigeminal nerve (control rat), with 12-keV x-rays, voxel size 5.4 μm, slice thickness 5.4 μm. The slices were calculated from a measured 3D data set of densities and are parallel to the plane of histological sections made before tomography. The distances of the left and right slice, respectively, to the sectioning plane are 70 μm and 150 μm. The scale of 1 mm applies in vertical and horizontal directions. Density values were converted into colors using the color bar given at the top. Yellow corresponds to nerve and blue to brain tissue. Light violet is the paraffin used as embedding material. Note the nerve fibers (NF) following the nerve axis. Some of the nerve fibers cross the brain/nerve boundary (BF). Areas of highest density (HD) are found notably close to the nerve surface. The horizontal pattern is an artifact due to air bubbles captured at the nerve-paraffin interface during the embedding process. In Table 1 density values in various parts of the tomograms are listed. Referring to the single nerve fibers that can be seen within the nerve, the fiber *position* is denoted by ① and the *interval* between fibers by ②. Locations at the *edge* of the nerve are marked ③.

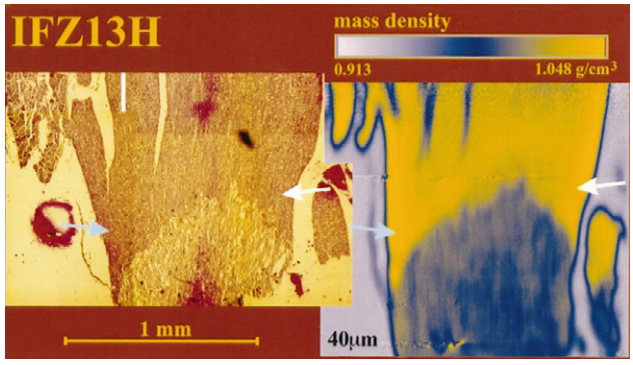

FIGURE 3 As Fig. 2 except that the tomogram (*right*) is shown together with the histological section (*left*) of the trigeminal nerve of a rat ~20 days after exposure to EtNU on postnatal day 1. Cell nuclei are visible in the section image as dark spots. They appear to be more crowded at the left and right edge of the nerve, regions which would correspond to areas of higher mass density (i.e., more saturated yellow) in the tomogram at the right (*arrows*), although this correspondence is only partly convincing. It has to be taken into account that the plane of the tomogram is separated from the plane of the histologic section by 40 μm. Note the match between the *shape* of the brain/nerve boundary in either picture. The analysis of the density data compiled in Table 1 shows that the overall density of the nerve part of this tomogram is ~14 mg/cm^3 higher than in the case of the control specimen not previously treated with EtNU, which is shown in Fig. 2.

the nerve axis. Cylindrical specimens of 2–5 mm in diameter and ~4 mm long were then prepared on a small lathe. To the extent practically possible, the nerve axis was also made the rotation axis of tomography, i.e., the *z*-axis in Fig. 1. From the tomographic 3D data-set, slices parallel to the surfaces caused by sectioning were calculated.

RESULTS AND DISCUSSION

The goal of the present study was to investigate to what extent small structural alterations in the tissue of a peripheral nerve can be visualized by p-μCT. In particular we wanted to see whether early stages of carcinogen-induced tumor development can be detected in the immature peripheral nervous system (PNS) of rats by employing phase contrast. Since cell nuclei, because of their content of phosphorus, have higher mass density than cell plasma, regions with a higher number density of cell nuclei due to tumor growth should have increased average mass density. Consequently, on phase contrast tomograms, nerve tissue containing micro tumors in the early growth stage might become detectable through its higher mass density. Therefore, we compared the intracranial segments of trigeminal nerves of rats exposed to the carcinogen *N*-ethyl-*N*-nitrosourea (EtNU) on postnatal day 1 (Nikitin et al., 1991, 1996) at an early stage of tumor development with those of an unexposed control animal.

As an example, we show a series of tomograms of rat trigeminal nerve specimens of animals not exposed (Fig. 2) and exposed (Figs. 3 and 4) to EtNU. In the images yellow

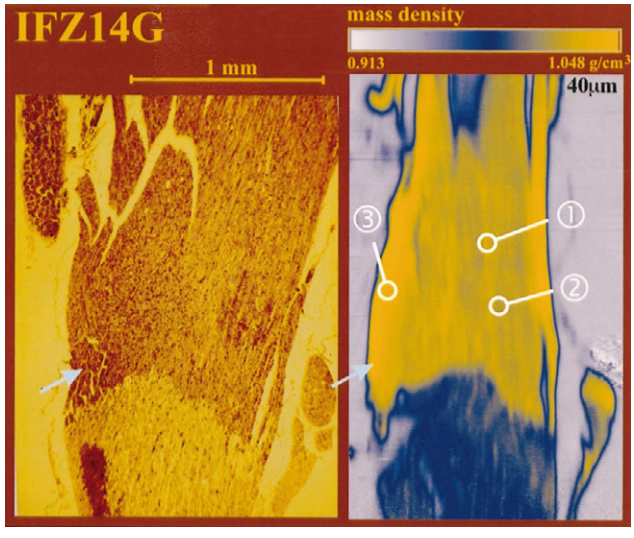

FIGURE 4 As Fig. 3, except for representing a different animal that was also exposed to EtNU. Again ①, ②, and ③ mark locations of fiber positions, intervals between fibers, and more dense regions near the nerve edge, respectively. The arrow points to a region where increased number density of cell nuclei in the section image corresponds to higher mass density in the tomogram. The analysis of the density data compiled in Table 1 shows that the overall density of the nerve part of this tomogram is ~12 mg/cm^3 higher than in the case of the control specimen not previously treated with EtNU, which is shown in Fig. 2.

corresponds to nerve tissue, dark blue to brain tissue, and light violet to the embedding paraffin. Horizontal bands of sharp contrast are artifacts caused by air bubbles trapped at the tissue/paraffin interface during the embedding process. The measured primary data are 3D charge- or, as stated in Eq. 6b, mass-density distributions. However, in order to simplify and ease evaluation, *numbers* of density values were converted into *colors* according to the color bar given at the top of the figures. It should be noted that no manipulation (e.g., by some arbitrary color table) is involved in this conversion. Local mass densities can be evaluated from colors within the same and also between different pictures in a *quantitative* way since the same color table was used in all cases. At the same time it always remains possible to work directly from number values of density again if this should be required, for instance, by interesting structural details in the image.

Fig. 2 shows two different tomographic slices obtained from a control animal. The left and right slices are located inside the nerve at ~70 and 150 μm, respectively, below the flat surface resulting from sectioning. The brain/nerve (b/n) border is very well delineated. Single nerve fibers ~15–30 μm thick are visible inside the nerve tissue (NF in Fig. 2) and, in a few cases, also extending into the brain (BF in Fig. 2). The latter is more pronounced in the tomogram at the left in Fig. 2 (70 μm distance from the sectioning surface), probably because this slice as a whole is close to the 3D b/n boundary. Regions of higher density are seen near the nerve surface (HD in Fig. 2). The higher density could be due to the perineural sheath, although the general shape of the higher density regions and their absence in other surface locations does not confirm this. Figs. 3 and 4 show histological sections (*left*) together with tomograms (*right*) of trigeminal nerves of two different rats with early stages of tumor development after carcinogen exposure. The tomograms were taken of the same nerve region at a depth of 40 μm below the sectioning plane. In the histological section the brain is of lighter color than the nerve tissue. The matching of histological sections and tomograms is particularly evident from the outline of the b/n interface on pictures of the same specimen. Due to the distance of 40 μm between tomogram and section, the correspondence is not complete. Cell nuclei, which in histological sections are visible as darker spots, appear to be increased in number near the left nerve edge in Figs. 3 and 4, and close to the b/n interface in Fig. 3 (*arrows*). Increased cell nuclei density is known to result from the uncontrolled proliferation of premalignant and malignant cells. In the tomograms these regions are more yellow, indicative of higher mass density. Furthermore, judging from the overall color of the exposed specimens in Figs. 3 and 4, their density is higher than that of the unexposed specimen (Fig. 2).

To express these findings more quantitatively, we have compiled in Table 1 density data from different parts of the specimens. All values are measured at ~1 mg/cm^3 SE. Referring to the single nerve fibers within the nerve the density was measured at the *fiber position* ① and at the *interval* ② between fibers. A third value was taken at the nerve *edge* ③. In Figs. 2–4 typical locations where these values apply are denoted by ①, ②, and ③, respectively. Furthermore, we calculated the *fiber contrast* (defined as the density difference at locations ① and ②), and the *average* of values taken at ①, ②, and ③. All numbers are obtained separately for the nerve tissue (at left in Table 1) and the adjacent brain tissue (at right in Table 1).

Very close to the nerve edge the density appears to be increased in all animals, regardless of their carcinogen-exposed or control status. The data also show that measured average densities in the trigeminal nerve for exposed versus control rats are 1033 mg/cm^3 and 1020 mg/cm^3, respectively. For exposed rats the trigeminal nerve is thus found to be ~13 mg/cm^3 more dense overall. For the adjacent brain tissue this difference is 4 mg/cm^3, i.e., only slightly higher than the present detection limit for density changes (2 mg/cm^3). The fiber contrast in either tissue is ~16 mg/cm^3. Furthermore, the b/n interface appears more diffuse in exposed rats.

We have thus demonstrated that by employing the method of p-μCT it has become possible to investigate structurally important details even in light specimens through mapping density changes of the order of 2 mg/cm^3. The information achieved is *truly three-dimensional* in the sense that the final result represents a data set of density values of all voxels in a cylindrical sample *volume* of typically 2 to 5 mm in diameter and up to 10 mm in length. The application of p-μCT indicates that the appearance of early atypical proliferates in the trigeminal nerves of rats previously exposed to EtNU (Swenberg et al., 1975; Nikitin

TABLE 1 Mass density (mg/cm^3) of trigeminal nerves of untreated control rat (row 2) and of rats exposed to EtNU (rows 3 and 4).

		Nerve tissue					Adjacent brain tissue				
Row (Fig.)	Rat	① Fiber Position	② Fiber Interval	③ Nerve Edge	Fiber Contrast	Average	① Fiber Position	② Fiber Interval	③ Nerve Edge	Fiber Contrast	Average
2	Control	1023	1004	1034	19	1020.3	993	977	999	16	989.7
3	Exposed	1035	1021	1048	14	1034.7	999	984	1004	15	995.7
4	Exposed	1031	1017	1048	16	1032.0	997	980	1002	17	993.0

Primary data, measured at 1 mg/cm^3 SE, are listed in columns ①, ②, and ③, which correspond to different locations in the specimen as indicated in Figs. 2–4 and here. Fiber contrast is column ① minus ②. Average is the average of columns ①, ②, and ③. Note that in the nerve tissue (adjacent brain tissue) averages are ~14 mg/cm^3 (5 mg/cm^3) larger for exposed rats than for the control animal, respectively.

et al. 1991, 1996) is reflected by density increases in the affected nerve tissue amounting to ~10 mg/cm^3 at ~20 days after carcinogen exposure on postnatal day 1.

The authors thank W. Drube, H. Schulte-Schrepping, and R. Treusch of beam line BW2 of HASYLAB at DESY, Hamburg, and Å. Kvick of beam line 2/ID11 at ESRF, Grenoble, France.

Financial support by the Bundesminister für Bildung und Forschung, BMBF, Bonn, under contract No. 05 SPEAAB1, by the Minister für Wissenschaft und Forschung, NRW, Düsseldorf, and by the Dr. Mildred Scheel Stiftung für Krebsforschung, Bonn, is gratefully acknowledged.

REFERENCES

Beckmann, F. 1998. Entwicklung, Aufbau und Anwendung eines Verfahrens der Phasenkontrast-Mikrotomographie mit Röntgen-Synchrotronstrahlung. Ph.D. thesis, University of Dortmund, Germany.

Beckmann, F., U. Bonse, F. Busch, and O. Günnewig. 1997. X-ray microtomography (μCT) using phase contrast for the investigation of organic matter. *J. Comput. Assist. Tomogr.* 21:539–553.

Beckmann, F., U. Bonse, F. Busch, O. Günnewig, and T. Biermann. 1995. A novel system for x-ray phase-contrast microtomography. *HASYLAB Jahresbericht II*:691–692.

Bonse, U., F. Beckmann, M. Bartscher, T. Biermann, F. Busch, and O. Günnewig. 1997. Phase-contrast x-ray tomography using synchrotron radiation. *Proc. SPIE.* 3149:108–119.

Bonse, U., and F. Busch. 1996. X-ray computed microtomography (μCT) using synchrotron radiation (SR). *Prog. Biophys. Mol. Biol.* 65:133–169.

Bonse, U., and M. Hart. 1965. An x-ray interferometer with long separated interfering beam paths. *Appl. Phys. Lett.* 7:99–100.

Borrmann, G. 1950. Die Absorption von Röntgenstrahlen im Fall der Interferenz. *Zeitschr. Physik.* 127:297–323.

James, R. W. 1967. The optical principles of the diffraction of x-rays. G. Bell and Sons, London.

Kak, A. C., and M. Slaney. 1987. Principles of computerized tomographic imaging. IEEE Press, New York.

Momose, A., T. Takeda, and Y. Itai. 1995. Phase-contrast x-ray computed tomography for observing biological specimens and organic materials. *Rev. Sci. Instrum.* 66:1434–1436.

Neumüller, O.-A. 1973. Römpps Chemie-Lexikon. Franckh'sche Verlagshandlung, Stuttgart.

Nikitin, A. Yu, L. A. P. Ballering, J. Lyons, and M. F. Rajewsky. 1991. Early mutation of the neu (erbB-2) gene during ethylnitrosourea-induced oncogenesis in the rat Schwann cell lineage. *Proc. Natl. Acad. Sci. USA.* 88:9939–9943.

Nikitin, A. Yu, J.-J. Jin, J. Papewalis, S. N. Prokopenko, K. M. Pozharisski, E. Winterhager, A. Flesken-Nikitin, and M. F. Rajewsky. 1996. Wild type neu transgene counteract mutant homologue in malignant transformation of rat Schwann cells. *Oncogene.* 12:1309–1317.

Swenberg, J. A., N. Clenendon, R. Denlinger, and W. A. Gordon. 1975. Sequential development of ethylnitrosurea-induced neurinomas: morphology, biochemistry and transplantability. *J. Natl. Cancer Inst.* 55:147–152.